Ferromagnetic and antiferromagnetic orders of a phase-separated manganite probed throughout the *B-T* phase diagram

Y. W. Windsor,[1] Yoshikazu Tanaka,[2] V. Scagnoli,[1,3] M. Garganourakis,[1] R. A. de Souza,[1] M. Medarde,[4] S.-W. Cheong,[5] and U. Staub[1]

[1]*Swiss Light Source, Paul Scherrer Institut, 5232 Villigen PSI, Switzerland*
[2]*RIKEN SPring-8 Center, Sayo, Hyogo 679-5148, Japan*
[3]*Laboratory for Mesoscopic Systems, Department of Materials, ETH Zurich, 8093 Zurich, Switzerland*
[4]*Laboratory for Scientific Developments and Novel Materials, Paul Scherrer Institut, 5232 Villigen PSI, Switzerland*
[5]*Rutgers Center for Emergent Materials and Department of Physics & Astronomy, Rutgers University, Piscataway, New Jersey 08854, USA*

We employ resonant soft x-ray diffraction (RSXD) to isolate the signal from the CE-type antiferromagnetic phase of $(La,Pr)_{1-x}Ca_xMnO_3$ (with $x \approx 3/8$), and follow only this phase through the known phases of the material in the *B-T* phase diagram. This material is known to exhibit a range of electronic ordering phenomena, most notably a metal-insulator transition (associated with colossal magnetoresistance) and phase separation between the antiferromagnetic phase and a ferromagnetic phase. Bulk magnetization measurements under the same *B-T* conditions were also conducted, giving a full picture of both phases for direct side-by-side comparison. The comparison specifically focuses on the metal-insulator transition. Upon magnetic field ramping to this transition, we find that the CE-type order undergoes a sharp quench at high temperatures (above phase coexistence temperatures) but that at lower temperatures, where the CE order is metastable, the transition broadens significantly. At the lowest temperatures, where a spin glass-type phase is expected, a slow annihilation of remanent CE domains is observed. Finally, a refined phase diagram is presented.

I. INTRODUCTION

Controllable material properties are highly sought after in solid-state physics due to the prospect of future novel applications. Over the past few decades, major discoveries were made in doped materials, including high-T_C superconductivity in doped cuprates and colossal magnetoresistance (CMR) in manganites, where doping was used to reach mixed-valence states (i.e., Mn^{3+} and Mn^{4+} sites in the same compound). These mixed-valence manganites exhibit a variety of phases, ranging from room-temperature ferromagnetic metals and ferromagnetic insulators to charge ordered and orbitally ordered (CO and OO) antiferromagnets. These fundamentally different electronic ordering phenomena appear at the same doping level for different manganite families. For example, with a calcium doping level of $x = 3/8$, the material $La_{1-x}Ca_xMnO_3$ (LCMO) exhibits a ferromagnetic metallic (FMM) phase [1], while $Pr_{1-x}Ca_xMnO_3$ (PCMO) exhibits a CO/OO/antiferromagnetic (AF) phase (known as the CE phase [2]) [Fig. 1(a)]. Schematics of these two materials' phase diagrams are shown in Fig. 1(b), with the $x = 3/8$ range highlighted.

To further manipulate the electronic behavior, one can tune the chemical pressure by substituting a fraction of the rare earth ions with slightly smaller or larger ones. In this manner, a hybrid of LCMO and PCMO can be produced, described as $La_{1-x-y},Pr_yCa_xMnO_3$ (LPCMO). Here, the mixing of La and Pr is expressed using the parameter y, while the overall Ca doping is still described using x. LPCMO was shown to exhibit a wealth of electronic phenomena in a single material, including phase separation and spin glass-type freezing of competing magnetic phases [4–6], evidence of the disorder in the system. The most prominent feature observed is magnetic-field switching between a CO/OO/AF insulating phase and

a FMM phase, the transition associated with CMR. This transition is strongly hysteretic at high temperatures, but at low temperatures it becomes irreversible, in concomitance with the appearance of dynamic phase separation, in which the areas of CO/OO/AF and FMM phases coexist [7,8]. LPCMO has also attracted recent attention in attempts to manipulate its properties at the nanoscale [9] and using magnetoelectric coupling [10].

The main boundaries of LPCMO's *B-T* phase diagram, including the spin glass phase, have been mapped out using standard magnetization and electron transport measurements in Refs. [6,7,11]. Such measurements are sensitive to the FMM phase but provide no information about the CO/OO/AF phase. This is especially problematic when phase separation occurs, because the limited CO/OO/AF volume bears little influence upon the FMM signals. The CO/OO/AF phase was inadvertently observed using magnetic imaging techniques, but only as an absence of the FMM signal [7,8].

A study that did directly access this phase was presented in recent years by Burkhardt *et al.* [8], in which resonant soft x-ray diffraction (RSXD) was used. RSXD is an ideal technique for studying LPCMO, because the resonant signal enhancement allows it to retain sensitivity to even minute sample volumes [12]. This allows following of the CO/OO/AF phase, even when it is almost entirely quenched by the FMM phase. Burkhardt *et al.* [8] provided key information regarding the irreproducibility of the CO/OO/AF phase upon cooling and heating. However, because no magnetic field was applied, much of the CO/OO/AF phase's behavior was not observed. A similar zero-field experiment was presented by García-Muñoz *et al.* [13].

Here, we present a RSXD study of $La_{\frac{2}{8}}Pr_{\frac{3}{8}}Ca_{\frac{3}{8}}MnO_3$ ($x = y = 3/8$) under magnetic fields of up to 4 T, which allows
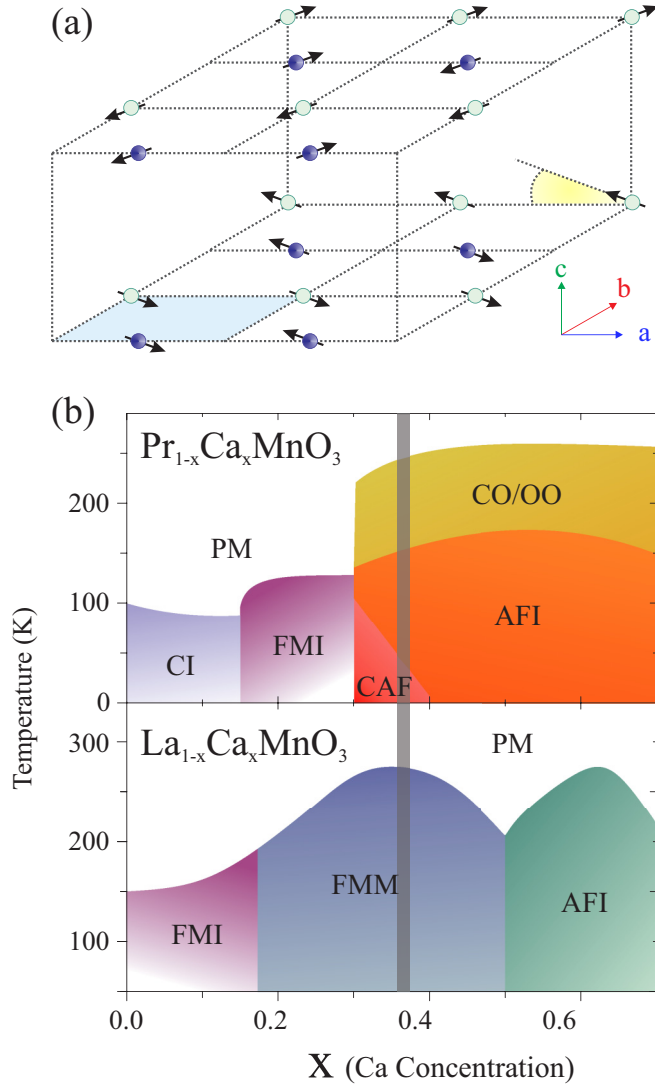
FIG. 1. (a) Diagram of the CE order, with only Mn ions presented. Different ion shadings indicate different Mn valance states. The diagram takes into account the c axis canting away from the pure CE type, expected for $0.3 < x < 0.5$. As such, all spin directions indicated are in the ac plane. A shaded region at the bottom of the diagram is a projection of the unit cell on the ab plane. The canting angle is indicated for one Mn moment. (b) Schematic phase diagrams of PCMO and LCMO as functions of doping, based on Refs. [1,3], respectively. The notations FMI, CI, AFI, and CAF denote ferromagnetic insulator, spin-canted antiferromagnetic, antiferromagnetic insulating, and canted antiferromagnetic states, respectively.

following of the CO/OO/AF phase throughout the known B-T phase diagram. This allows us to directly probe the CO/OO/AF phase, both as the dominant phase and as a minuscule fraction of the total sample volume. Magnetization measurements were conducted on the same sample, so the results can be directly related to the expected behavior of the FMM phase. The aims of this paper are to observe the AF order under low temperatures and high magnetic fields and to compare its behavior to that of the FMM order under the same conditions.

The nomenclature related to the metal-insulator transition in this material varies widely in literature as authors focused on different aspects of it (e.g., its association with CMR). Several authors refer to it as the metal-insulator transition, but others refer to it as the supercooling and superheating transitions [7]. Because the transition can be crossed throughout the B-T phase diagram by varying either B or T (explicitly shown in Ref. [7]), we refer to both as G, with G^* as the CO/OO/AF to FMM transition and G^{**} as the reverse transition. These boundaries are explicitly shown in the phase diagram below. Other transitions are $T_{CO/OO}$, T_N, T_g, and T_C, which correspond to the appearance of the CO/OO order, the AF order, the spin glass transition and the spontaneous appearance of the FMM order, respectively.

II. EXPERIMENTS

The LPCMO single crystals were grown in an optical floating-zone furnace at Rutgers University and were cut and polished to produce a (100)-oriented surface. Laue characterization of crystals indicate that the a and b lattice constants are close in size, so crystal twinning can occur. High-field RSXD measurements were conducted using an upgraded diffractometer based on the prototype instrument [14] at the beamline 17SU [15] in the SPring-8 synchrotron radiation source. A superconducting cryomagnet of fields reaching 4 T can be mounted in the diffractometer. In this experiment, a 1.0×0.5 mm^2-sized beam of left-handed circularly polarized light was used. This size is much larger than the average domain size [4,7,8]. The RSXD measurements in zero field were conducted using the RESOXS ultrahigh vacuum diffraction end station [16] at the SIM beamline [17] of the Swiss Light Source (SLS). In this case, linearly polarized incident light was used, with either π or σ polarization (electric field in the scattering plane or perpendicular to the scattering plane, respectively). In both experiments, photon energies used correspond to the Mn $L_{2,3}$ absorption edges ($2p \rightarrow 3d$, $\sim$643 and $\sim$652 eV), directly probing the Mn $3d$ electronic states. Samples were mounted on the cold head of a flow cryostat and cooled to temperatures as low as 5 K. Rotation of the sample around the momentum transfer vector $\boldsymbol{Q}$ (azimuthal rotation; see the experimental geometry in Fig. 2) was conducted in zero field using a mechanical arm to a precision of $\pm 5°$. For all results herein, the azimuthal angle Ψ is defined as zero when the crystallographic $\hat{b}$ axis is in the scattering plane. The direct current (dc) magnetization measurements were conducted using a commercial Physical Property Measurement System (PPMS) device equipped with a 9-T superconducting magnet and the Alternating Current Measurement System (ACMS) option.

III. RESULTS

A. Resonant soft x-ray diffraction in zero field

RSXD was used to study the ($^1/_2$ 0 0) reflection (Pbnm notation) at the Mn $L_{2,3}$ edges. The energy dependence of this reflection's intensity is presented in Fig. 3. The temperature evolution of the integrated intensity from this reflection is presented in Fig. 4(a) upon warming. This reflection is expected to probe the magnetic order, and indeed intensity appears below
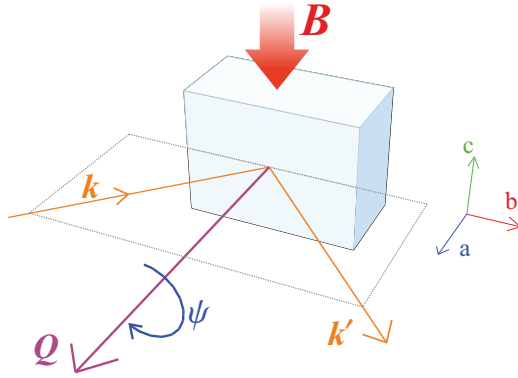
FIG. 2. Sketch of the RSXD experiment. The incoming and outgoing directions k and k' define the scattering plane. The momentum transfer $Q = k' - k$ is also indicated, as is the azimuthal rotation angle Ψ. We define $\Psi = 0°$ when the b axis is in the scattering plane (crystal axes are shown for this case). The magnetic field B is applied when $\Psi = 0°$, along the c axis direction.

$T_N \approx 190$ K. The inset of Fig. 4(a) presents a close-up at high temperatures, which was taken at a different azimuthal angle and spot on the sample. Here, an additional weak contribution to intensity already appears below $T_{(CO/OO)} \approx 215$ K and is therefore attributed to the appearance of orbital (and charge) order. However, orbital order should follow a $(0 \frac{1}{2} 0)$ ordering wave vector. We therefore assume that this contribution is from a twinned part of the sample, which can occur because the a and b lattice constants are nearly identical, which allows $(0 \frac{1}{2} 0)$ and $(\frac{1}{2} 0 0)$ to overlap in reciprocal space. The data in Fig. 4(a) show no intensity above 190 K, and are over three times more intense than the inset's data at all temperatures below 185 K. Therefore, we conclude that at the photon energy used, the magnetic intensity is dominant over the orbital contribution from the twinned part of the sample.
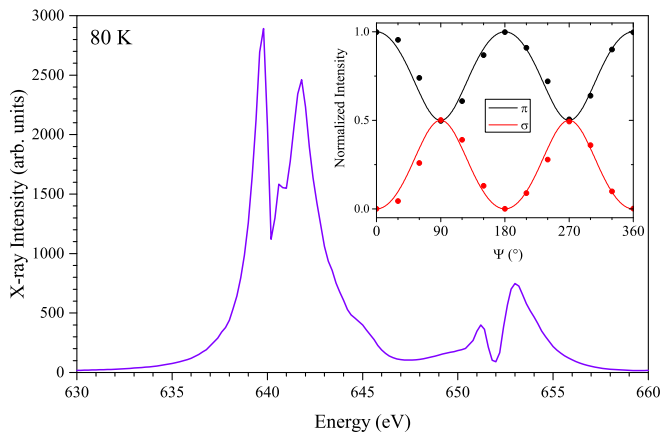

FIG. 3. Energy dependence of the peak intensity of the $(\frac{1}{2} 0 0)$ reflection at 80 K at $\Psi = 90°$. Inset: integrated intensity of the same reflection upon azimuthal rotation (see geometry in Fig. 2). Circles represent intensity for π and σ incoming polarizations, normalized by the sum of intensities $(I_\pi + I_\sigma)$. Solid lines are calculations of the expected intensity from a CE-type structure with a nonzero canting angle, based on Ref. [18].
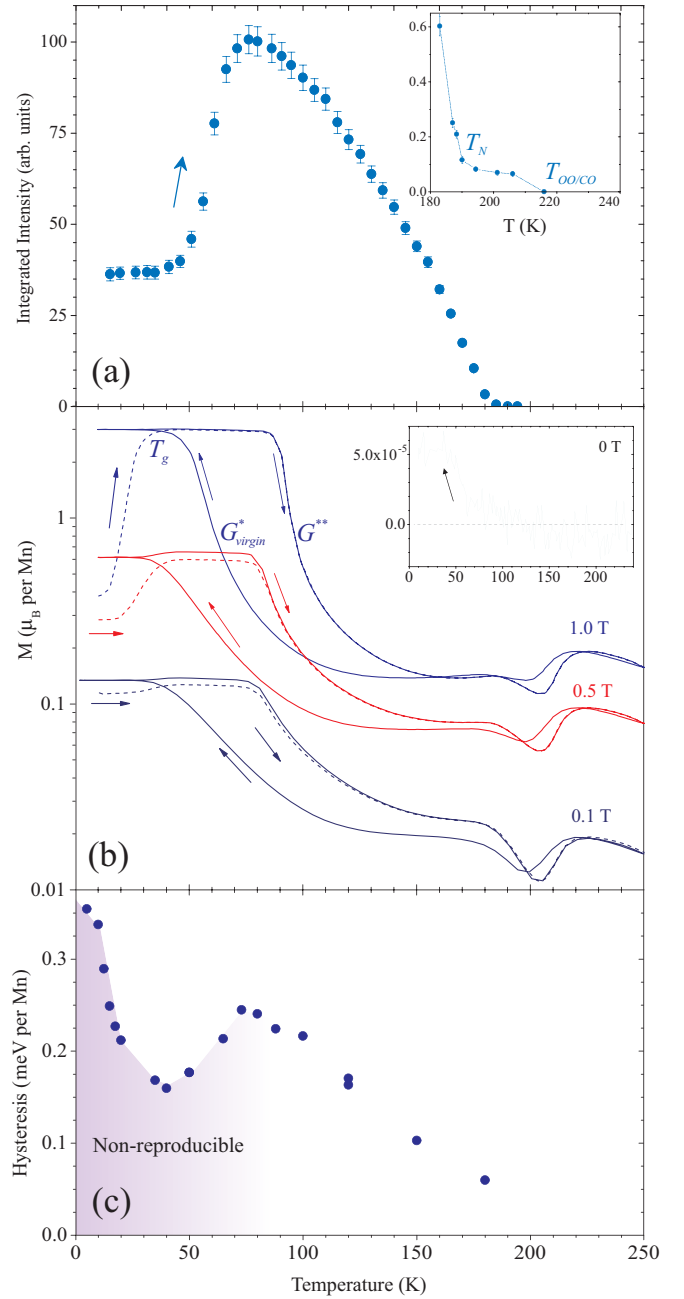

FIG. 4. (a) Integrated RSXD intensity of the $(\frac{1}{2} 0 0)$ reflection as a function of temperature upon warming (after ZFC), recorded using 644 eV π-polarized linear light. Data were recorded after ZFC at $\Psi = 0°$. Inset: high-temperature data recorded with $\Psi = 90°$; the Neel temperature and the onset of OO/CO are indicated. (b) Magnetization upon heating and cooling under three exemplary magnetic fields. Lines represent heating-cooling cycles in an applied field. Dashed lines represent field heating after ZFC. Inset: ZFC. The G^*_{virgin}, G^{**}, and T_g transitions are indicated for the 1-T curves. (c) Energy per Mn atom of the magnetic hysteresis as measured for different temperatures [Fig. 7(c)].

The main feature observed in Fig. 4(a) is a rise in intensity around 60 K upon heating. This is due to the change in the mixing ratio between the FMM and the CO/OO/AF phases (i.e., change of scattering volume), which are known to
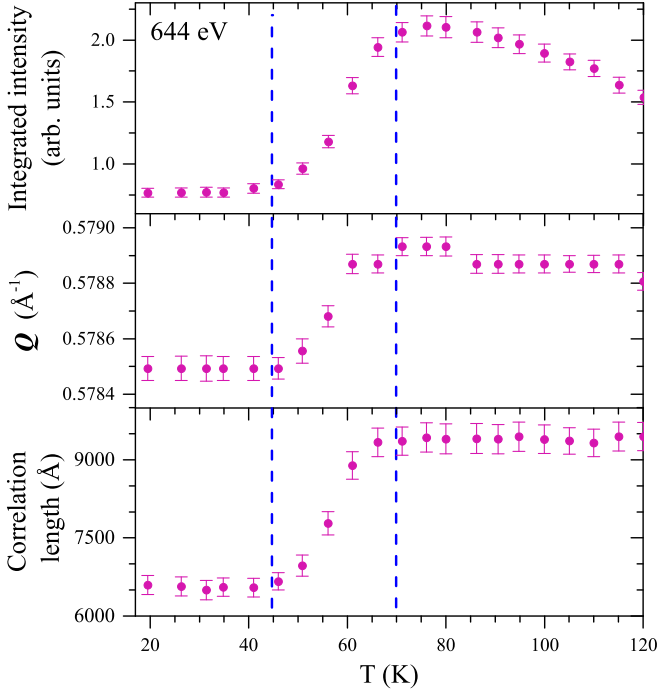
FIG. 5. Temperature dependence of the integrated intensity, momentum transfer Q, and correlation length around 60 K. Data were recorded after ZFC.

FIG. 6. Rocking curves around the $(\frac{1}{2}\,0\,0)$ reflection, measured at 5 K, under different magnetic fields.

have slightly different crystal structures [13]. This is shown alongside magnetization data in Fig. 4(b) and 4(c), as function of the same temperature scale. Figure 5 presents the integrated intensity, the correlation length ($2\pi/$FWHM, where FWHM denotes full width at half maximum), and the momentum transfer around 60 K. All features show a sharp change at the same temperature, in qualitative agreement with the behavior found for LPCMO with a slightly different mixing parameter y in Ref. [8]. LPCMO is not known to undergo a significant change in the lattice constants at this temperature, and it is not expected to acquire any incommensurate order [13]. A small monoclinic distortion is known to occur with charge ordering, which may cause the shift in Q around the 60 K transition [19,20]. The change in correlation length agrees with the existence of phase-separated competing orders at lower temperatures.

The resonant magnetic structure factor can be written within the approximation of a dipolar transition as

$$F = (\hat{\varepsilon}' \times \hat{\varepsilon}) \cdot \sum_i \boldsymbol{m}_i e^{2\pi i \boldsymbol{Q} \cdot r_i} \qquad (1)$$

in which $\hat{\varepsilon}$ and $\hat{\varepsilon}'$ are the incident and scattered polarization directions and $\hat{m}$ and r are the direction of magnetization and position of the ith resonant ion, respectively. Plugging the CE-type AF magnetic structure [21] into Eq. (1), we find that the $\boldsymbol{Q} = (\frac{1}{2}\,0\,0)$ reflection should not exhibit magnetic intensity. However, between doping levels of $x = 0.3$ and 0.5, PCMO is known to acquire varying spin canting along the c axis [18], in addition to the pure CE-type AF order [18,21] [Fig. 1(a)]. The periodicity of this additional component is induced by the CE-type order, and it is this addition to the magnetic structure that contributes to the intensity of $(\frac{1}{2}\,0\,0)$. To demonstrate this, the
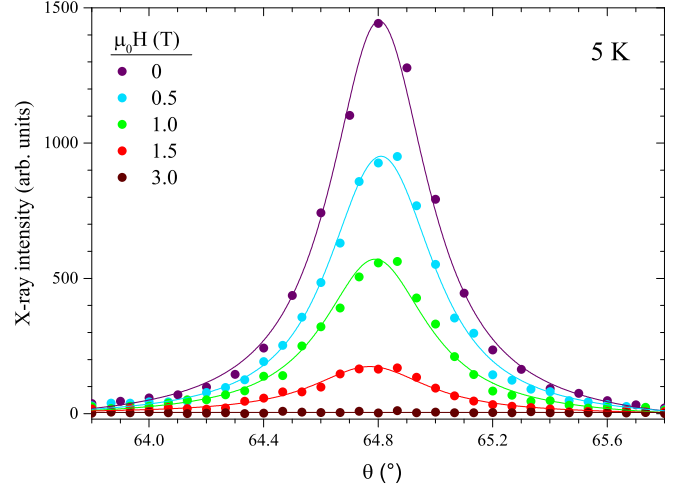
azimuthal dependence of this reflection is presented in the inset of Fig. 3. The expected intensity from the magnetic structure with the additional canting was calculated using Eq. (1) and is plotted over the data. Good agreement is found between the calculation and the data, and we therefore conclude that the intensity of the magnetic $(\frac{1}{2}\,0\,0)$ reflection is sensitive to the c axis canting only.

B. Resonant soft x-ray diffraction in magnetic fields

The intensity of the same $(\frac{1}{2}\,0\,0)$ reflection was studied as a function of applied magnetic fields. Figure 6 presents rocking curves of this reflection as function of magnetic field at 5 K [22]. The peak shape does not vary substantially through the G^* transition, which reduces the intensity. Therefore, in subsequent data, we choose to follow only the peak height as a function of the magnetic field, not its integrated intensity.

In all experiments, magnetic fields were applied along the c axis. During field-dependent measurements (both RSXD and dc magnetization), the following experimental procedure was conducted [see the sketch in Fig. 7(a)]. The sample is cooled from room temperature to a desired temperature. The field is ramped up and down at this temperature, resulting in a "virgin curve." The sample is then heated up to 120 K. All subsequent field ramping is conducted after cooling from 120 K. All field ramping cycles at $T \geqslant 120$ K were conducted after a field ramping cycle at $T < 120$ K. This procedure ensured the reproducibility of results.

Figure 7(b) presents the peak intensity as a function of the applied field, ramped at different temperatures at a rate of ~ 3 mT/s. The main feature is a drop of intensity at $H = G^*$, above which the signal is completely quenched. This is notably different from the temperature-dependent drop observed for zero field in Fig. 4(a) (around 60 K), where some CO/OO/AF regions remain at lower temperatures. The shape of the curve varies substantially between temperatures: in scans taken for $T \geqslant 50$ K, we find that the intensity remains constant up to G^*, while for $T < 50$ K, the curve is rounded and the transition is broader. This indicates a change from a single, well-ordered AF state at high T to a collection of small domains with a
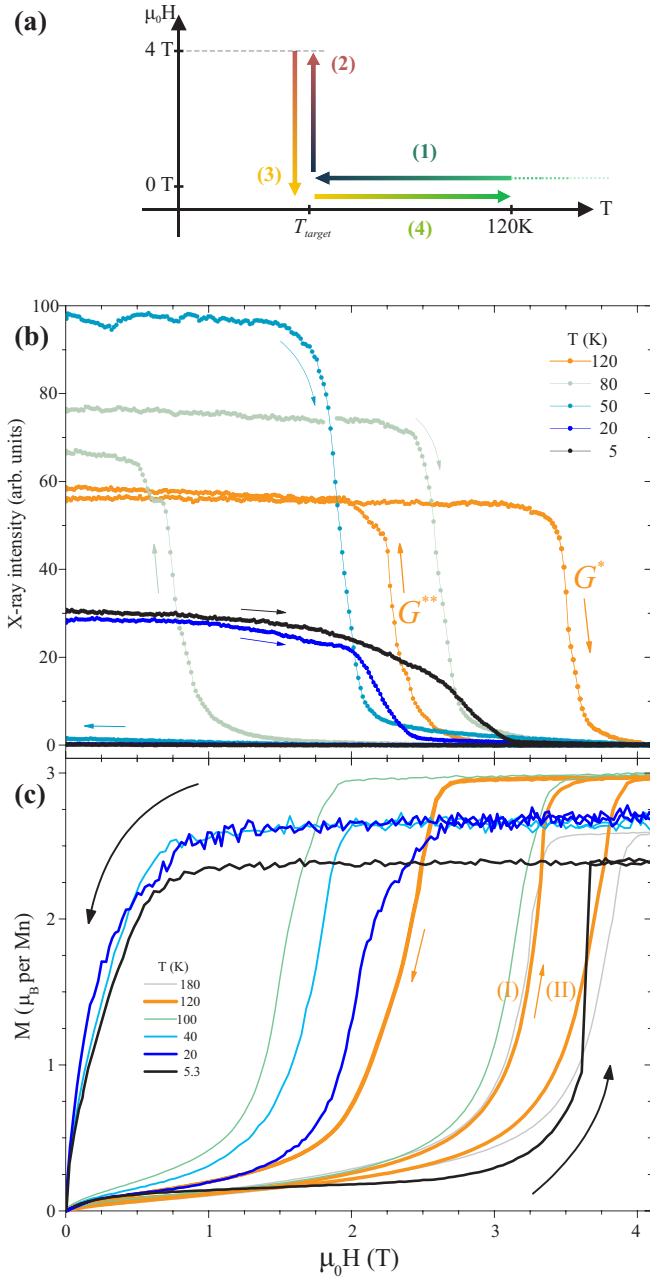
FIG. 8. X-ray intensity from the $(\tfrac{1}{2}\,0\,0)$ reflection at two temperatures within the glass phase (left axis, in log scale) and applied magnetic field (right axis), both presented as functions of elapsed time. The dashed line is a guide for the eye.

Figure 8 presents two RSXD curves measured as the field is ramped up in the same procedure but as functions of time. The applied field is also presented on the same scale. At these temperatures, LPCMO is in the spin glass phase. Two regimes of reversal are clearly observed. The earlier regime accounts for most of the signal suppression and becomes less sharp as the temperature is reduced. In the second regime, the RSXD signal appears to decay independently of the applied field, and the RSXD signals from 5 K and 20 K coincide. By fitting these data to a decay function of the simple exponential form exp-(t/τ), we find $\tau \approx 633$ s.

C. Magnetometry

For a complete picture of magnetic behavior, we follow the magnetization of the sample under the same conditions as in the RSXD experiment. Figure 7(c) presents $M(H)$ at different temperatures (at 120 K, two field cycles are shown: a virgin cycle and a subsequent cycle). The rise in magnetization at higher fields is the G^* transition to the FMM phase (indicated by an arrow). Before it, a weak rise in magnetization is observed, most likely from areas of imperfection in the crystal. Upon ramping the field down, the G^{**} transition back into the CO/OO/AF phase is observed for the high-temperature curves. For 40 K and 20 K, the recovery is at near-zero field. This is in accord with the loss of RSXD recovery below ∼65 K. Because the size and shape of the hysteresis curve vary strongly with temperature, Fig. 4(c) presents the average energy associated with the Mn ions (calculated using the area of the hysteresis loop, the lattice constants, and the crystal's mass). This is a measure of the latent energy associated with the first-order transition between the CO/OO/AF phase and the FMM phase.

Figure 4(b) presents $M(T)$ upon field cooling (FC) and field warming in $\mu_0 H = 0.1, 0.5$, and 1 T. Field warming is shown both after FC and after zero-field cooling (ZFC). A ZFC curve is shown in the inset, indicating that a small ferromagnetic moment is present due to the appearance of spontaneous magnetization. Comparison between curves for

FIG. 7. (a) Sketch of the experimental procedure for subsequent field ramping. (b) peak intensity as function of magnetic field, ramped at different temperatures. Curves shown below 80 K exhibit no hysteretic recovery. The transitions G^* and G^{**} are indicated for the 120 K data. (c) field-dependent magnetization as function of magnetic field. For 120 K, the virgin and the subsequent ramping up of the field are indicated by I and II, respectively.

broad distribution of energy barriers at low T. When the field is ramped back down, the opposite transition occurs at $H = G^{**}$. For $T \geqslant 100$ K, a full recovery of the intensity is observed at $H = G^{**}$ (not shown). For $T \leqslant 50$ K, no G^{**} transition is observed when ramping H down, and the intensity does not recover. In the range between these, a partial recovery of intensity is observed at $H = G^{**}$ (a recovery of a few percent is still observed at 65 K).
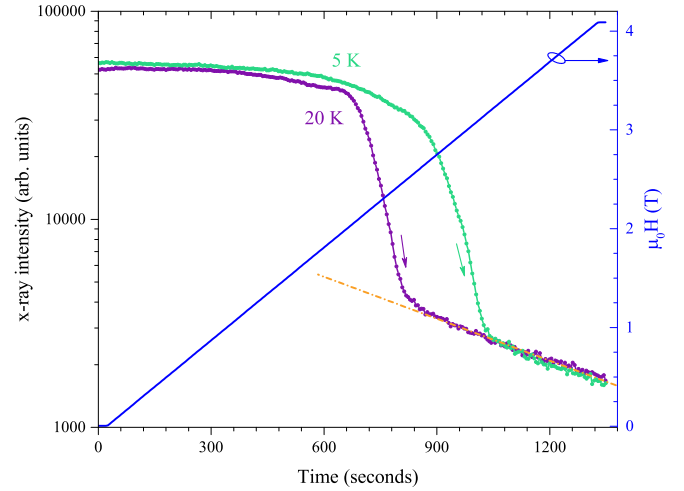
1 and 0.5 T indicates that both the magnitude of $M(T)$ and the transition temperatures are field dependent. In all cases, the cooling began at 250 K, well above all transitions. The feature at 210 K is a signature of the border between the paramagnetic (PM) and the CO/OO/AF phases. This signature consists of two transitions at $T_{OO/CO}$ and T_N [seen in Fig. 4(a)]. Below T_N, the initial rise of the cooling curve marks the appearance of FMM domains at T_C. The sharp rise of the FC curve is at $T = G^*_{virgin}$, which is the transition of the system from CO/OO/AF to the FMM phase (the virgin subscript indicates that cooling is from above T_N). This transition is interrupted by the glass transition T_g (unless $H > 2$ T). Upon field-heating from within the glass phase, a further rise in $M(T)$ is observed, likely due to melting of the spin glass into the FMM phase. This is followed by the G^{**} transition from the FMM phase back into the CO/OO/AF phase, closing a hysteresis loop as a function of temperature.

The value of T_g is commonly taken as the temperature at which the ZFC and FC warming curves merge. However, in applied magnetic fields, these curves do not necessarily coincide. For example, at $H = 0.5$ T, the ZFC and FC curves differ by more than 10% in magnetization outside the glass phase [Fig. 4(b)]. This can be understood within the picture of a hierarchy of energy barriers, which persist outside the glass phase [11]. For this reason, we mark the glass transition here as the middle of the characteristic rise in magnetization when entering the FMM phase upon warming. This rise occurs at different temperatures in the ZFC and FC warming curves (designated T_g and the T_g', respectively). The T_g' value remains constant with the applied field, while the T_g value reduces with higher applied magnetic fields.

Lastly, we note that although the observed moment appears to behave paramagnetically in fields on the scale of $H = G^{**}$, ferromagnetic hysteresis is indeed observed. To show this, the system was cooled to 5.3 K, and the field was then ramped up to 5 T and back down to 0 T to ensure that no CO/OO/AF islands remain. A series of low-field hysteresis curves around $B = 0$ T was recorded at various temperatures upon warming. Figure 9 presents the remanent magnetization at zero field as a function of temperature, and the inset presents one such
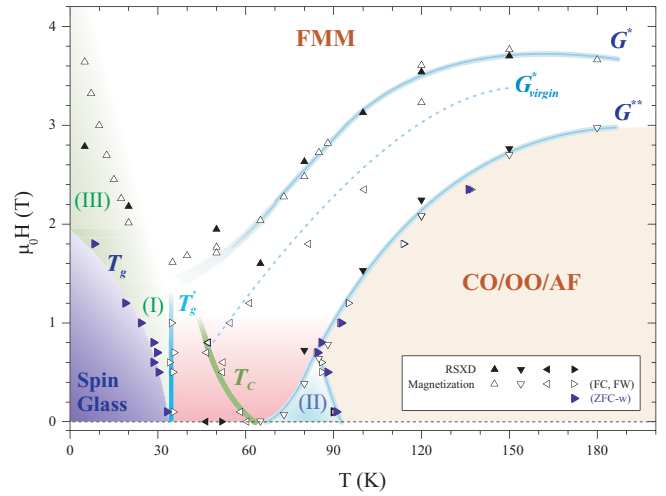
FIG. 10. Phase diagram drawn from transition temperatures found in RSXD and magnetization measurements. The shaded region around the T_C line indicates the region where phase coexistence reportedly occurs. The regions labeled I and II are explained in the main text. The region labeled III above the spin glass phase marks the discrepancy between field ramping measurements and those taken upon cooling or heating. This is due to slow relaxation dynamics, so transitions upon field ramping are therefore not used to define the T_g or G^* boundaries at the lowest temperatures.

hysteresis curve. We find that $T_C(H = 0) \approx 110$ K, indicating that the field-ramping procedure in Fig. 7(a) is adequate.

D. Phase diagram

Here, we revisit the phase diagram of LPCMO. Previous less detailed reports have drawn this diagram without taking into account probes that are directly sensitive to the AF order [6,7]. The phase diagram is presented in Fig. 10. Data points indicate positions of transitions, the orientation of the triangular markers indicates the ramp direction in which the transition appears (magnetic field is up and down, and temperature is left and right), and their filling indicates the technique used.

The most prominent features are the G^* and G^{**} transitions. In addition, a line labeled G^*_{virgin} is traced within the hysteretic region between G^* and G^{**}. This line indicates where the G^* transition occurs when the sample is cooled directly from room temperature (in contrast to the main G^* line, which is observed after reheating to above 120 K) [Fig. 7(a)]. It intersects with the line labeled T_C, which begins where spontaneous magnetization appears upon cooling in zero field (the spontaneous appearance of FMM domains). This virgin behavior reproduces in all experiments and agrees with the first-order nature of the G^* transition, in which domains may coexist and act as nucleation sites, facilitating a faster transition or one that requires a lower coercive field. However, it is unclear what the nature of these nucleation sites is, because the FMM phase is not expected to exist at temperatures well above T_C.

The shaded region in the center of the diagram (around the T_C line) indicates the region where dynamic phase coexistence reportedly occurs [4,7,8]. Here, we observe the highest
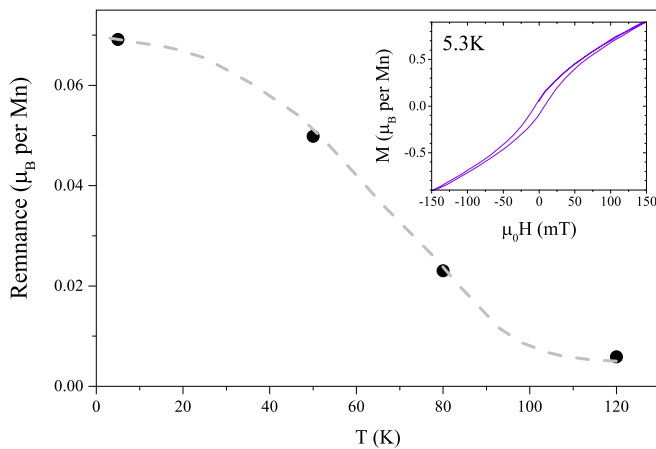

FIG. 9. Remanent magnetization as a function of temperature. The line is a guide for the eye. Inset: hysteresis loop at 5.3 K after saturating the system at 5 T.

RSXD magnetic intensity. We identify this region by the disappearance of the G^{**} transition and the irreproducibility of the CO/OO/AF phase: after the field is ramped above $H = G^*$, the RSXD signal does not recover at all. This underlines the metastability of the phase coexistence. The borders of this region are obscure, because they are highly hysteretic.

Directly adjacent is T_g, indicating the transition from the spin glass to the FMM phase. It is shown twice: T_g and T_g' (the rise in magnetization in the ZFC and FC measurements, respectively). The difference between them (indicated by I in the phase diagram) grows with the applied field.

Also adjacent to the phase coexistence region is the region labeled II, a narrow pocket below the FMM phase, centered around 80 K. It is characterized by partial recovery of the CO/OO/AF phase following the G^{**} transition. Its borders are defined by an inconsistency between the position of the G^{**} transition when the field is ramped down and that upon warming. This partial recovery is demonstrated in Fig. 11. Figure 11(a) presents an RSXD hysteresis loop at 80 K. Following the G^{**} transition, only ~90% of the magnetic intensity recovers. Figure 11(b) presents a magnetization experiment under the same conditions. Here, however, the field is ramped up a second time. The second hysteresis curve is 15% smaller in area than the first. This is consistent with the partial recovery of the CO/OO/AF phase (in the previous cycle), because less field needs to be invested to quench the CO/OO/AF phase. Furthermore, this confirms observations of partial recovery of magnetic hysteresis in Ref. [7].

IV. DISCUSSION

Measuring the RSXD signal under applied fields (Figs. 6 and 7) helps to clarify the behavior of the CO/OO/AF phase. The $(\frac{1}{2} 0 0)$ signal is sensitive only to the canted c axis magnetic components, which alternate in direction from site to site. This additional component is associated with excess electron density at doping levels of $0.3 < x < 0.5$. Assuming the field (applied along the c axis) strengthens and weakens those components parallel and antiparallel to it, respectively, the intensity would not change as a function of the magnetic field, as long as the AF modulation amplitude remains constant. This is a direct result from Eq. (1). The intensity does reduce when the scattering volume decreases, which for $T > 50$ K occurs abruptly at $H = G^*$, indicating a collective quenching of the AF modulation. The magnetization measurements in Fig. 7(c) confirm this scenario, because the rise in net moment is minor below $H = G^*$. Below T_C, the RSXD signal exhibits a different magnetic field dependence. It does not remain constant up to G^* but instead gradually reduces as the field is applied (in other words, the RSXD hysteresis curve is not sharp but rounded). This indicates a reduction in scattering volume due to the gradual appearance of FMM domains, which become favorable as the field is applied.

A remark related to the stability of the CO/OO/AF phase should be made. Figure 12 presents G^*, G^{**}, and the integrated intensity of the $(\frac{1}{2} 0 0)$ reflection as functions of temperature. The transition fields weaken as temperature is reduced, down to a temperature range in which the CO/OO/AF order is metastable. This behavior serves as an indicator for the
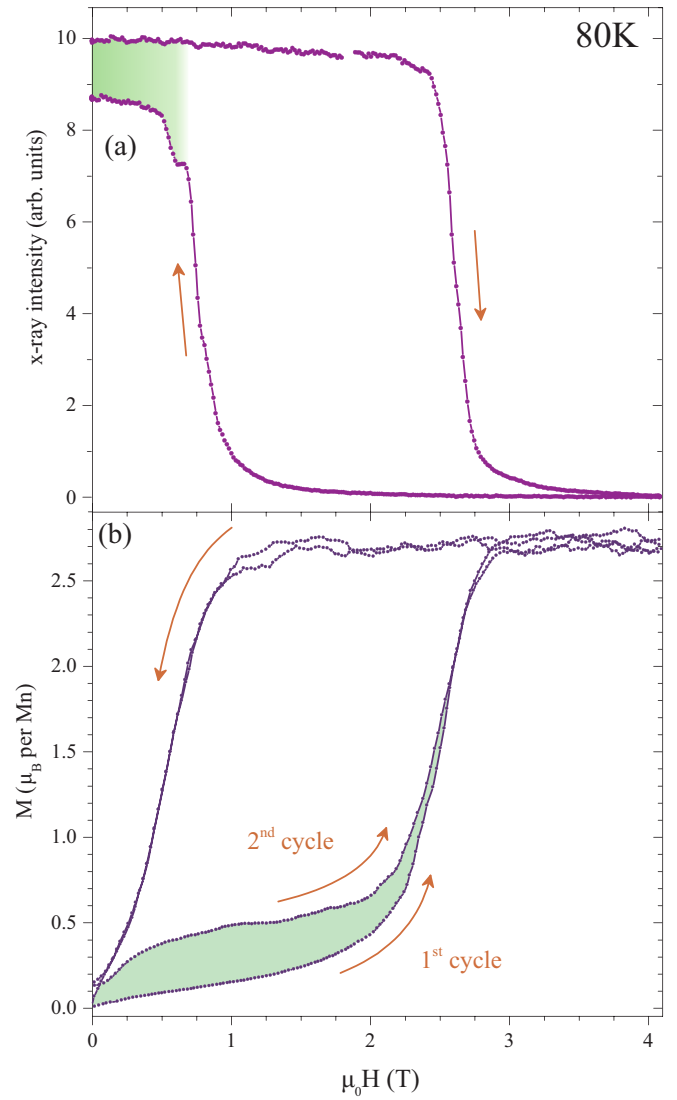

FIG. 11. (a) Diffracted intensity from the $(\frac{1}{2} 0 0)$ reflection, measured as a function of the applied magnetic field at 80 K. Upon ramping the field down, the intensity does not fully recover. (b) Magnetic moment as a function of the applied field, measured at 80 K. Two consecutive cycles were recorded, which are found to be inequivalent. In both panels, the highlighted region indicates the partial recovery of the CO/OO/AF phase.

weakening of the CO/OO/AF orders (or their associated exchange terms) in favor of the FMM phase. However, in the same temperature range, the integrated intensity rises, indicating an increase in the magnetic order parameter associated with the c axis spin canting upon cooling. This increase in intensity can also be due to an increase in the c axis canting angle [Fig. 1(a)]. Following Jirak *et al.* in Ref. [18], this would be analogous to an effective decrease in Ca doping in PCMO (reduction of x). This discrepancy between the increase in intensity and the reduction in transition fields (upon cooling) suggests that the two magnetic components (CE order and c axis spin canting) have different magnetic susceptibilities or that they are weakly coupled to each other. Nevertheless, once the main CE-type order is quenched, electron mobility rises sharply [4], quenching the c axis modulation as well.
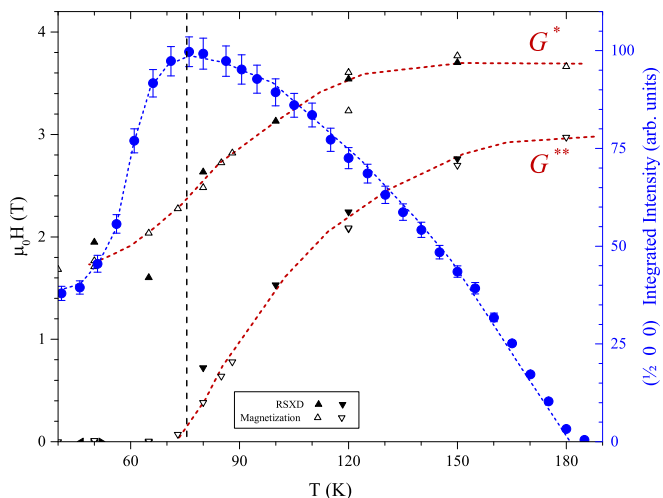
FIG. 12. The G^* and G^{**} transition fields as functions of temperature (left axis) and the integrated intensity from the $(\frac{1}{2}\,0\,0)$ reflection (right axis). Dashed lines are guides for the eyes; the vertical dashed line indicates that the temperature of peak RSXD intensity coincides with the temperature at which G^{**} vanishes.

The spin glass transition is known to occur upon cooling through the spontaneous appearance of the FMM phase [7], essentially freezing it alongside the metastable CO/OO/AF phase. The balance between the two coexisting phases during the glass transition depends on the field applied. This is apparent in the difference between the FC and the ZFC warming curves [Fig. 4(b)]. Nevertheless, the glass phase continues to relax over time, as evidenced by very slow magnetic dynamics, which have been explained as a result of a hierarchy of energy barriers [11]. Although FC tips the system toward favoring the FMM phase, the $T_g{'}$ line occurs at higher temperatures than the T_g line (the transitions from within spin glass upon warming after FC and ZFC, respectively). This means that preference of the FMM phase stabilizes the glass phase.

When the field is ramped up from within this phase, the decay of the RSXD signal exhibits two distinct behaviors (Fig. 8). The first is the rounded behavior previously described, which is due to a gradual reduction of scattering volume. This is responsible for quenching almost all of the signal. The second regime is a slow exponential decay, which appears insensitive to the field applied. This can be understood as a slow decay (or annihilation) of remanent CO/OO/AF domains surrounded by an FMM environment. While a simple exponential can reasonably describe the decay, further studies on this phase are required to identify the correct form of the decay, such as those already proposed for spin glasses in Refs. [23–25]. These would indicate whether such a FM-AF system agrees with the known temporal behavior of spin glasses. Nevertheless, the longevity of these CO/OO/AF islands can explain the slow magnetic relaxation observed in previous studies and variations in the relaxation speeds [11]. Slow relaxation causes a discrepancy between data taken upon cooling or warming and data taken upon field ramping. The shaded region labeled III in Fig. 10 marks this discrepancy. Due to this effect, we extrapolate the T_g line in the phase diagram (Fig. 10) without

considering the transitions recorded using field ramps at the lowest temperatures.

Persistent slowly annihilating domains are a known effect in ferromagnets. A model describing their effect on subsequent magnetization reversals is presented in Ref. [26]. While this model can be applied to the present scenario, the nature of the interaction between the two domain types in LPCMO remains unclear.

V. SUMMARY

In conclusion, we have employed RSXD to study the CO/OO/AF order of LPCMO at low temperatures and high magnetic fields, covering the entire phase diagram. Magnetization measurements were used to follow the coexisting FMM phase under the same conditions. Additional elements of the phase diagram were presented and discussed. The use of RSXD allowed us to observe small volumes of the CO/OO/AF phase coexisting within the FMM phase.

The RSXD signal is sensitive not to the main CE-type magnetic order but to the alternating c axis spin canting. For temperatures above the phase separation, the signal remains constant with the applied field and vanishes sharply at the CMR transition (at $H = G^*$), indicating a collective quenching of the CO/OO/AF order. When FMM domains are present, applying a field reduces the RSXD signal even before the G^* transition, indicating a growth of the FMM order at the expense of the AF order. Furthermore, below T_c, phase separation occurs also at zero field and when the metal-insulator transition becomes irreversible with field (i.e., no recovery transition G^{**}), and the system must be heated to retain its CO/OO/AF phase. During this metastable condition, in which the CO/OO/AF order is weakest, the RSXD signal is most intense. This suggests that the antiferromagnetically modulated c axis canting and the main CE order have different magnetic susceptibilities, because it appears that the magnetic field does not directly couple to the c axis component but instead couples to the main CE-type order.

We find persistent (nonvolatile) behavior for both phases. The FMM phase persists to higher temperatures when it is produced by lowering T instead of ramping the field. Small CO/OO/AF domains survive at very high fields when applied within the spin glass phase and exhibit a slow annihilation process. It is yet unclear how the two phases interact, but both phases clearly bear evidence of a complex energy landscape with soft and hard energy barriers. A microscopic model to describe the wealth of phenomena exhibited by LPCMO will be immensely valuable for understanding control of electronic ordering.

[1] P. Schiffer, A. P. Ramirez, W. Bao, and S.-W. Cheong, Phys. Rev. Lett. **75**, 3336 (1995).

[2] E. O. Wollan and W. C. Koehler, Phys. Rev. **100**, 545 (1955).

[3] S. Y. Zhou, Y. Zhu, M. C. Langner, Y.-D. Chuang, P. Yu, W. L. Yang, A. G. Cruz Gonzalez, N. Tahir, M. Rini, Y.-H. Chu, R. Ramesh, D.-H. Lee, Y. Tomioka, Y. Tokura, Z. Hussain, and R. W. Schoenlein, Phys. Rev. Lett. **106**, 186404 (2011).

[4] M. Uehara, S. Mori, C. H. Chen, and S.-W. Cheong, Nature **399**, 560 (1999).

[5] H. J. Lee, K. H. Kim, M. W. Kim, T. W. Noh, B. G. Kim, T. Y. Koo, S.-W. Cheong, Y. J. Wang, and X. Wei, Phys. Rev. B **65**, 115118 (2002).

[6] P. A. Sharma, S. Baek Kim, T. Y. Koo, S. Guha, and S.-W. Cheong, Phys. Rev. B **71**, 224416 (2005).

[7] W. Wu, C. Israel, N. Hur, S. Park, S.-W. Cheong, and A. de Lozanne, Nat. Mater. **5**, 881 (2006).

[8] M. H. Burkhardt, M. A. Hossain, S. Sarkar, Y.-D. Chuang, A. G. Cruz Gonzalez, A. Doran, A. Scholl, A. T. Young, N. Tahir, Y. J. Choi, S.-W. Cheong, H. A. Dürr, and J. Stöhr, Phys. Rev. Lett. **108**, 237202 (2012).

[9] T. V. A. Nguyen, A. N. Hattori, Y. Fujiwara, S. Ueda, and H. Tanaka, Appl. Phys. Lett. **103**, 223105 (2013).

[10] M. Zheng and W. Wang, J. Appl. Phys. **119**, 154507 (2016).

[11] L. Ghivelder and F. Parisi, Phys. Rev. B **71**, 184425 (2005).

[12] E. Weschke, H. Ott, E. Schierle, C. Schüßler-Langeheine, G. Kaindl, V. Leiner, and H. Zabel, Phys. B **357**, 16 (2005).

[13] J. L. García-Muñoz, A. Collado, M. A. G. Aranda, and C. Ritter, Phys. Rev. B **84**, 024425 (2011).

[14] T. Takeuchi, A. Chainani, Y. Takata, Y. Tanaka, M. Oura, M. Tsubota, Y. Senba, H. Ohashi, T. Mochiku, K. Hirata, and S. Shin, Rev. Sci. Instrum. **80**, 023905 (2009).

[15] H. Ohashi *et al.*, in *Ninth International Conference on Synchrotron Radiation Instrumentation*, edited by J.-Y. Choi and S. Rah, AIP Conf. Proc. No. 879 (AIP, New York, 2007), p. 523.

[16] U. Staub, V. Scagnoli, Y. Bodenthin, M. García-Fernández, R. Wetter, A. M. Mulders, H. Grimmer, and M. Horisberger, J. Synchrotron Radiat. **15**, 469 (2008).

[17] U. Fleschig, F. Nolting, A. Fraile Rodriguez, J. Krempasky, C. Quitmann, T. Schmidt, S. Spielmann, and D. Zimoch, in *10th International Conference on Radiation Instrumentation*, edited by R. Garrett, I. Gentle, K. Nugent, and S. Wilkins, AIP Conf. Proc. No. 1234 (AIP, New York, 2010), p. 319.

[18] Z. Jirak, S. Krupica, Z. Simsa, M. Dlouha, and S. Vratislav, J. Magn. Magn. Mater. **53**, 153 (1985).

[19] R. J. Goff and J. P. Attfield, Phys. Rev. B **70**, 140404(R) (2004).

[20] E. E. Rodriguez, Th. Proffen, A. Llobet, J. J. Rhyne, and J. F. Mitchell, Phys. Rev. B **71**, 104430 (2005).

[21] M. v. Zimmermann, C. S. Nelson, J. P. Hill, D. Gibbs, M. Blume, D. Casa, B. Keimer, Y. Murakami, C.-C. Kao, C. Venkataraman, T. Gog, Y. Tomioka, and Y. Tokura, Phys. Rev. B **64**, 195133 (2001).

[22] The transition field is low in this dataset due to improper cycling of the temperature before acquisition [as in Fig. 7(a)].

[23] A. V. Gol'tsev, Zh. Eksp. Teor. Fiz. **91**, 1725 (1986).

[24] A. T. Ogielski, Phys. Rev. B **32**, 7384 (1985).

[25] R. M. Pickup, R. Cywinski, C. Pappas, B. Farago, and P. Fouquet, Phys. Rev. Lett. **102**, 097202 (2009).

[26] Y. W. Windsor, A. Gerber, I. Ya. Korenblit, and M. Karpovski, J. Appl. Phys. **113**, 223902 (2013).